Validation of a physically-based solid oxide fuel cell anode model combining 3D tomography and impedance spectroscopy

CrossMark

A. Bertei [a],[*], E. Ruiz-Trejo [a], F. Tariq [a], V. Yufit [a], A. Atkinson [b], N.P. Brandon [a]

[a] Department of Earth Science and Engineering, Imperial College London, SW7 2AZ, UK
[b] Department of Materials, Imperial College London, SW7 2AZ, UK

ARTICLE INFO

ABSTRACT

This study presents a physically-based model for the simulation of impedance spectra in solid oxide fuel cell (SOFC) composite anodes. The model takes into account the charge transport and the charge-transfer reaction at the three-phase boundary distributed along the anode thickness, as well as the phenomena at the electrode/electrolyte interface and the multicomponent gas diffusion in the test rig. The model is calibrated with experimental impedance spectra of cermet anodes made of nickel and scandia-stabilized zirconia and satisfactorily validated in electrodes with different microstructural properties, quantified through focused ion beam SEM tomography. Besides providing the material-specific kinetic parameters of the electrochemical hydrogen oxidation, this study shows that the correlation between electrode microstructure and electrochemical performance can be successfully addressed by combining physically-based modelling, impedance spectroscopy and 3D tomography. This approach overcomes the limits of phenomenological equivalent circuits and is suitable for the interpretation of experimental data and for the optimisation of the electrode microstructure.

Introduction

Solid oxide fuel cells (SOFCs) are electrochemical systems which convert the chemical energy of a fuel, such as hydrogen, directly into electric energy and heat, allowing for high efficiency of power generation [1,2], low emission of pollutants [3] and fuel flexibility [4]. The performance and durability of the cell are strongly dependent on the electrodes [5–7], which are porous layers, typically made of a composite of ceramics and/or metallic particles, wherein electrochemical reactions occur. There is significant interest in relating the electrode microstructure to electrochemical performance [8–12]. Understanding how the microstructure affects the electrochemical response would allow researchers to better design the electrodes to increase power density and extend lifetime [13–17].

This task can be accomplished by using physically-based models. Physically-based electrochemical models solve

conservation equations for charged and chemical species to provide a mechanistic description of the transport and reaction processes occurring within the electrodes [18–21]. The microstructural characteristics of the electrodes are included in the model with different levels of complexity. In some recent studies, model equations are solved within the three-dimensional microstructure of the electrode [22–24], which is reconstructed with tomographic techniques [25–28]. However, the computational cost of this type of simulations is currently too high to allow for a systematic use of this method. Typically, the continuum approach is adopted in developing electrochemical models [19,29–31]. In this approach the particle-level details are represented through effective microstructural properties, which can be obtained from the application of empirical correlations [32], percolation models [33–35], packing algorithms [36,37] or 3D tomography [38]. Several modelling studies have been presented to predict the microstructural contribution to electrochemical performance and enhance the power density via an optimisation of the microstructural properties [19,37,39–43].

However, in most of the studies published so far the validation of the model is lacking [32,44,45]. In order to quantify the correlation between microstructure and electrochemical performance, models must be properly calibrated with high-quality electrochemical experimental data and then verified in different electrode microstructures. Typically electrochemical models are calibrated by tuning microstructural or electrochemical parameters on a single set of polarization curves [30,46,47] without assessing their validity in different samples. Furthermore, electrochemical impedance spectroscopy (EIS) data contain more information than polarization curves and allow for the decoupling of different processes according to their characteristic timescale, thus representing a more comprehensive benchmark for the validation of electrochemical models [48–53].

This study describes the validation of a physically-based electrochemical model by using impedance spectroscopy data for different operating conditions and different electrode microstructures. The study focuses on SOFC composite anodes made of the same materials, nickel and scandia-stabilized zirconia (ScSZ), prepared with different volume fractions and fabrication techniques, including infiltrated electrodes. Focused ion beam SEM (FIB-SEM) tomography is used to obtain the microstructural parameters required by the model, while EIS data at different operating conditions are used for its calibration and validation. The results of the study comprise the material-specific kinetic parameters of Ni:ScSZ electrodes, which can be used along with the model to optimise the microstructural design.

The paper is organized as follows: in Section 2 the electrochemical model is presented. Section 3 reports the results of the study, comprising the fitting and deconvolution of impedance spectra, the discussion of model parameters and the cross verification of the model in different microstructures. The general conclusions of the study are reported in Section 4.

Modelling

Fig. 1a schematically represents the main phenomena occurring within the anodes modelled and tested in this study. The anode consists of a porous composite layer of Ni and ScSZ particles randomly dispersed and sintered on the top of an yttria-stabilized zirconia (YSZ) electrolyte [54]. Hydrogen is supplied to the anode and diffuses throughout the diffusive stagnant layer, which is expected to be present in electrodes tested in button cell configuration [55–57]. Hydrogen is electrochemically oxidized at the three-phase boundaries (TPBs) among Ni, ScSZ and pores spread throughout the thickness of the anode. Water counter-diffuses back while electrons migrate along the percolating electron-conducting networks created by Ni particles. Oxygen ions, coming from the electrolyte, are transferred to the ScSZ phase at the anode/electrolyte interface and then reach the TPBs to take part in hydrogen electro-oxidation.

The electrochemical model, developed in the next section, mathematically describes these transport and reaction phenomena. The following set of simplifying assumptions are considered in order to keep the model as simple as possible and reduce the number of unknown parameters:

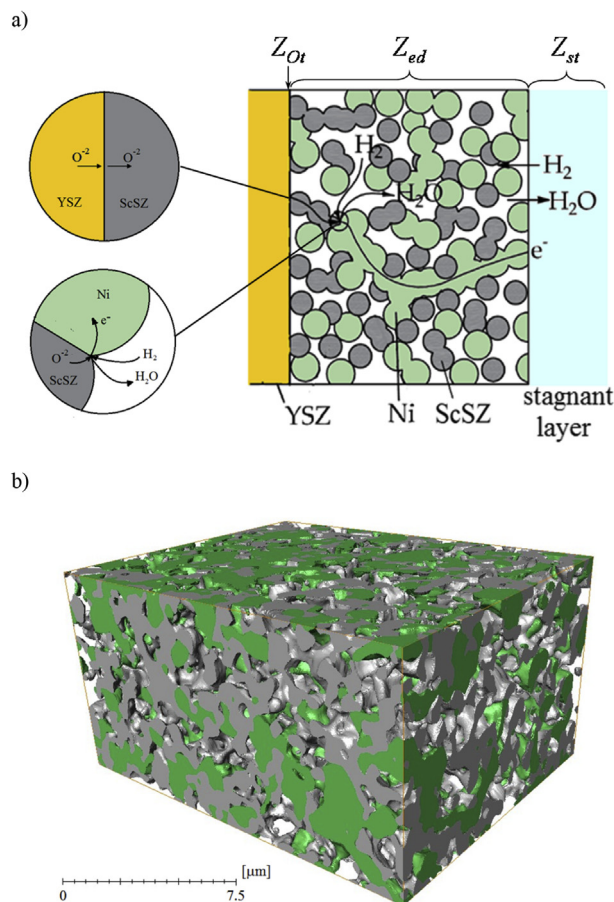**Fig. 1 – a) Schematic representation of the charge-transfer and charge transport phenomena occurring within the anode (not to scale). On the top, the three contributions to electrode impedance are reported. b) Tomographic reconstruction of the anode Ni40 (green: Ni, grey: ScSZ). (For interpretation of the references to colour in this figure legend, the reader is referred to the web version of this article.)**

- no mixed ionic-electronic conduction, i.e., Ni is regarded as a pure electronic conductor while ScSZ as a pure ionic conductor;
- charge-transfer reactions are described according to Butler-Volmer kinetic expressions [34,58];
- the gas transport within the pores of the anode is neglected due to the small thickness of the electrode. This assumption is further verified in Section 3.2 (see Fig. 5);
- isothermal conditions;
- only the transport and reaction phenomena occurring along the thickness of the electrode are modelled, resulting in a 1D distributed model. For the button cell configuration used here, this 1D approximation has been shown to be sufficient to extract accurate results [51,59,60];
- the electrode microstructure is modelled as a continuum: the effective microstructural properties, such as the TPB length per unit volume and the effective conductivities, which are evaluated from the tomographic reconstruction of the electrodes (see Fig. 1b), are assumed homogeneous throughout the electrode thickness.

Although the model is applied to Ni:ScSZ anodes, it is generally applicable to any type of composite SOFC electrodes that satisfy the assumptions listed above.

Model equations

According to the description provided in the previous section, the impedance of the electrode consists of three processes occurring in series (see Fig. 1a):

- oxygen ion transfer at the electrode/electrolyte interface;
- distributed charge-transfer at the TPB spread throughout the electrode thickness, coupled with electron and oxygen ion migration;
- gas diffusion in the stagnant layer.

In this section the impedance of the electrode is derived according to physically-based sub-models describing these processes. For the sake of conciseness, model equations are reported in the frequency domain only. The symbol $\Delta\zeta$ is used to represent the phasor of the a.c. perturbation of a generic variable ζ' around its steady-state value ζ, which is the open-circuit condition in this case:

$$\zeta' - \zeta = \delta\zeta \cdot e^{j(\omega t + \varphi)} = \Delta\zeta \cdot e^{j\omega t} \text{ with } \delta\zeta << \zeta \tag{1}$$

where j is the imaginary unit and ω the angular frequency, with $\omega = 2\pi f$, where f is the frequency. For a comprehensive description of the Fourier transformation of model equations from time domain to frequency domain the reader is referred to Lasia [61] and Bertei et al. [52].

The impedance of the oxygen ion transfer Z_{Ot} between YSZ and ScSZ at the electrode/electrolyte interface is represented through an oxygen transfer resistance $r_{ScSZ/YSZ}$ in parallel to a capacitance $c_{ScSZ/YSZ}$, as follows:

$$Z_{Ot} = \frac{1}{A_{ScSZ/YSZ}}\left(\frac{1}{r_{ScSZ/YSZ}} + j\omega c_{ScSZ/YSZ}\right)^{-1} \tag{2}$$

where $A_{ScSZ/YSZ}$ is the fraction of interfacial area between ScSZ and YSZ at the electrode/electrolyte interface. $r_{ScSZ/YSZ}$ is the

specific charge-transfer resistance associated to the Faradaic contribution of the oxygen ion transfer at ScSZ/YSZ interface, while $c_{ScSZ/YSZ}$ is a lumped parameter taking into account the double-layer capacitance and the other capacitive contributions associated to the oxygen ion transfer (oxygen ion transfer at the electrode/electrolyte interface is taken into account in several well-established physically-based models [62–64] and has been identified in the analysis of impedance spectra [52,65]).

The impedance related to the distributed charge-transfer at the TPB within the electrode is obtained from the conservation equations of electronic and ionic current along the thickness of the anode:

$$\begin{cases} \dfrac{d\Delta i_e}{dx} = -\Delta i^v_{TPB} - \Delta i^v_{Ni/ScSZ} \\[2mm] \dfrac{d\Delta i_O}{dx} = \Delta i^v_{TPB} + \Delta i^v_{Ni/ScSZ} \\[2mm] x = 0 : \Delta i_e = \Delta I, \Delta i_O = 0 \\[1mm] x = L_{an} : \Delta i_e = 0, \Delta i_O = \Delta I \end{cases} \tag{3}$$

where $x = 0$ refers to the electrode/current collector interface and $x = L_{an}$ to the electrode/electrolyte interface (i.e., from right to left in Fig. 1a). Note that the current perturbation ΔI is totally in electronic form at $x = 0$ while it is in ionic form at $x = L_{an}$ [34,42].

The electronic and ionic current densities, Δi_e and Δi_O respectively, are calculated according to Ohm's law [18–20]:

$$\Delta i_e = -\sigma^{eff}_{Ni}\frac{d\Delta V_{Ni}}{dx} \text{ with } \sigma^{eff}_{Ni} = \sigma_{Ni}k^{eff}_{Ni} \tag{4a}$$

$$\Delta i_O = -\sigma^{eff}_{ScSZ}\frac{d\Delta V_{ScSZ}}{dx} \text{ with } \sigma^{eff}_{ScSZ} = \sigma_{ScSZ}k^{eff}_{ScSZ} \tag{4b}$$

where σ^{eff}_{Ni} and σ^{eff}_{ScSZ} are the effective electronic and ionic conductivities of Ni and ScSZ, calculated by multiplying the bulk conductivity, σ_{Ni} and σ_{ScSZ}, by the normalized conductivity factor, k^{eff}_{Ni} and k^{eff}_{ScSZ} [20,37]. In Eq. (4), ΔV_{Ni} and ΔV_{ScSZ} represent the phasors of the electronic and ionic potential in Ni and ScSZ, respectively.

The source terms per unit volume in the right-hand side of Eq. (3) refer to the Faradaic current due to the charge-transfer reaction at the TPB Δi^v_{TPB} and the current associated to the electric double-layer between Ni and ScSZ $\Delta i^v_{Ni/ScSZ}$. According to the Butler-Volmer kinetics [58] and assuming ideal capacitive behaviour of the Ni/ScSZ interface [18], Δi^v_{TPB} and $\Delta i^v_{Ni/ScSZ}$ result as follows:

$$\Delta i^v_{TPB} = i_{0TPB}L^v_{TPB}\frac{F}{RT}(\Delta V_{Ni} - \Delta V_{ScSZ}) \tag{5a}$$

$$\Delta i^v_{Ni/ScSZ} = j\omega c_{Ni/ScSZ}A^v_{Ni/ScSZ}(\Delta V_{Ni} - \Delta V_{ScSZ}) \tag{5b}$$

where i_{0TPB} is the exchange current density per unit of TPB length, $c_{Ni/ScSZ}$ the specific capacitance of the Ni/ScSZ interface while L^v_{TPB} and $A^v_{Ni/ScSZ}$ are microstructural properties corresponding to the TPB length and the Ni/ScSZ contact area per unit volume, respectively. F, R and T represent the Faraday constant, the gas constant and the absolute temperature, respectively.

By defining the activation overpotential $\Delta\eta$ as [34]:

$$\Delta\eta = \Delta V_{Ni} - \Delta V_{ScSZ} \tag{6}$$

and introducing the dimensionless coordinate $\tilde{x} = x/L_{an}$, the substitution of Eqs. (4)–(6) into Eq. (3) provides the following system:

$$\begin{cases} \dfrac{d^2 \Delta\eta}{d\tilde{x}^2} = \Gamma^2 \Delta\eta \\[2mm] \dfrac{d\Delta\eta}{d\tilde{x}}\Big|_{\tilde{x}=0} = -\dfrac{L_{an}}{\sigma_{Ni}^{eff}}\Delta I \\[2mm] \dfrac{d\Delta\eta}{d\tilde{x}}\Big|_{\tilde{x}=1} = \dfrac{L_{an}}{\sigma_{ScSZ}^{eff}}\Delta I \end{cases} \quad (7)$$

where the dimensionless parameter Γ, which depends on frequency, is defined as:

$$\Gamma^2 = \left(i_{0TPB} L_{TPB}^v \frac{F}{RT} + j\omega c_{Ni/ScSZ} A_{Ni/ScSZ}^v \right) \left(\frac{1}{\sigma_{Ni}^{eff}} + \frac{1}{\sigma_{ScSZ}^{eff}} \right) L_{an}^2 \quad (8)$$

Eqs. (3)–(6) represent the extension to frequency domain of the steady-state model of porous composite SOFC electrodes proposed by Costamagna et al. [34], who provide the solution of Eq. (7) in order to compute the total overpotential of the electrode $\Delta\eta_{tot}$ as follows:

$$\begin{aligned} \Delta\eta_{tot} &= \Delta V_{Ni}|_{\tilde{x}=0} - \Delta V_{ScSZ}|_{\tilde{x}=1} \\ &= \frac{\cosh(\Gamma) + \Omega \cdot [2 + \Gamma \sinh(\Gamma) - 2\cosh(\Gamma)]}{\Gamma \sinh(\Gamma)} L_{an} \left(\frac{1}{\sigma_{Ni}^{eff}} \right. \\ &\quad \left. + \frac{1}{\sigma_{ScSZ}^{eff}} \right) \Delta I \end{aligned} \quad (9)$$

with:

$$\Omega = \frac{\sigma_{Ni}^{eff} \sigma_{ScSZ}^{eff}}{\left(\sigma_{Ni}^{eff} + \sigma_{ScSZ}^{eff} \right)^2} \quad (10)$$

Finally, the impedance of the electrode Z_{ed} due to the distributed charge-transfer reaction coupled with electron and ion migration is equal to:

$$\begin{aligned} Z_{ed} &= \frac{\Delta\eta_{tot}}{\Delta I} \\ &= L_{an} \left(\frac{1}{\sigma_{Ni}^{eff}} + \frac{1}{\sigma_{ScSZ}^{eff}} \right) \frac{\cosh(\Gamma) + \Omega \cdot [2 + \Gamma \sinh(\Gamma) - 2\cosh(\Gamma)]}{\Gamma \sinh(\Gamma)} \end{aligned} \quad (11)$$

It is noteworthy that Eq. (11) was also derived, with different notation, by Paasch et al. [66] and by Lasia [61], and is present in ZView (element DX-1) [67] to represent the impedance of an electrode with finite thickness and finite resistivity of the conducting phases. A modified version of Eq. (11) was also applied by Sonn et al. [68] and Ramos et al. [60] in Ni:YSZ and Ni:ScSZ cermet anodes, respectively. When the conductivity of a phase is much larger than that of the other one, Ω approaches 0 and Eq. (11) equals the impedance of a finite-length Gerischer element [61,69].

The multicomponent diffusion in the stagnant layer is described according to the Maxwell–Stefan approach [70]. In the following, a ternary mixture of H_2, H_2O and inert gas (e.g., N_2) is considered, where the species are labelled as 1, 2 and 3, respectively. The derivation that follows represents the extension to the frequency domain around OCV of the steady-state diffusion model proposed by Aravind et al. [57].

Under the assumption of uniform pressure P, the conservation equations for H_2 and H_2O within the stagnant layer read as follows:

$$\begin{cases} j\omega \dfrac{P}{RT}\Delta y_i = -\dfrac{d\Delta N_i}{dx} \\[2mm] \Delta y_i|_{x=0} = \Delta y_{i,0} \qquad \text{for } i = 1, 2 \\[2mm] \Delta y_i|_{x=L_{st}} = 0 \end{cases} \quad (12)$$

where, in this case, $x = 0$ represents the interface between electrode and stagnant layer while $x = L_{st}$ represents the thickness of the stagnant layer (i.e., from left to right in Fig. 1a). $\Delta y_{i,0}$ is the phasor of molar fraction, which is the a.c. perturbation generated by the dynamics of the electrochemical processes occurring within the electrode, which are assumed to be faster than the diffusion in the stagnant layer. The boundary condition at $x = L_{st}$ sets a constant molar fraction of H_2 and H_2O in the supply of gases outside the stagnant layer where the perturbations vanish, thus resulting in $\Delta y_i = 0$.

The phasor of the molar flux ΔN_i is computed according to the Maxwell–Stefan approach [70]:

$$-\frac{P}{RT}\frac{dy_i}{dx} = \sum_{k \neq i}^{3} \frac{y_k N_i - y_i N_k}{D_{ik}} \quad (13)$$

where D_{ik} is the binary diffusivity between species i and k, calculated according to the Fuller et al. equation [71]. Considering that, at steady-state, the reaction stoichiometry sets $N_2 = -N_1$ and $N_3 = 0$, the flux expression can be recast in a Fick-type form as [57]:

$$\Delta N_i = -\frac{P}{RT} D_i \frac{d\Delta y_i}{dx} \quad \text{with} \quad D_i = \left(\frac{y_1}{D_{12}} + \frac{y_2}{D_{12}} + \frac{y_3}{D_{i3}} \right)^{-1} \text{ for } i = 1, 2 \quad (14)$$

where the a.c. perturbation Δy_i in D_i has been neglected. In particular, D_i represents the average diffusivity of species i within the stagnant layer in open-circuit conditions.

By substituting Eq. (14) into Eq. (12), two independent second-order ordinary differential equations are obtained, whose solution is:

$$\Delta y_i(x) = \Delta y_{i,0} \frac{\sinh\left((L_{st} - x)\sqrt{j\omega/D_i} \right)}{\sinh\left(L_{st}\sqrt{j\omega/D_i} \right)} \quad (15)$$

By substituting Eq. (15) into Eq. (14), the phasor of the flux is obtained:

$$\Delta N_i|_{x=0} = \frac{P}{RT} D_i \frac{\sqrt{j\omega/D_i}}{\tanh\left(L_{st}\sqrt{j\omega/D_i} \right)} \Delta y_{i,0} \quad (16)$$

which is related to the a.c. current density ΔI experienced by the electrode according to the hydrogen oxidation reaction stoichiometry:

$$\Delta I = -2F\Delta N_1|_{x=0} = 2F\Delta N_2|_{x=0} \quad (17)$$

Eqs. (16) and (17) link the phasors of the molar fractions $\Delta y_{i,0}$ to the a.c. current density ΔI.

Following the Taylor expansion of the Nernst equation of hydrogen oxidation reaction, the a.c. perturbation of the

concentration overpotential at the interface between electrode and stagnant layer results as [72]:

$$\Delta\eta_{conc} = \frac{RT}{2F}\left(\frac{\Delta y_{2,0}}{y_2} - \frac{\Delta y_{1,0}}{y_1}\right) \quad (18)$$

By substituting Eqs. (16) and (17) into Eq. (18), the impedance contribution due to the diffusion within the stagnant layer Z_{st} results as follows:

$$
\begin{aligned}
Z_{st} &= \frac{\Delta\eta_{conc}}{\Delta I} \\
&= \left(\frac{RT}{2F}\right)^2 \frac{1}{P}\left(\frac{1}{D_1 y_1}\frac{\tanh\left(L_{st}\sqrt{j\omega/D_1}\right)}{\sqrt{j\omega/D_1}}\right. \\
&\quad \left. + \frac{1}{D_2 y_2}\frac{\tanh\left(L_{st}\sqrt{j\omega/D_2}\right)}{\sqrt{j\omega/D_2}}\right)
\end{aligned}
\quad (19)
$$

It is worth noting that Eq. (19) represents the sum of two finite-length Warburg elements [69], which is consistent with the mathematical description of H_2 and H_2O diffusion within a finite stagnant layer.

Finally, the total impedance of the system Z is calculated by summing up all the contributions:

$$Z = j\omega L_{cables} + R_{ey} + 2\cdot(Z_{Ot} + Z_{ed} + Z_{st}) \quad (20)$$

where the factor 2 takes into account that there are two anodes in the symmetric setup considered in this study, R_{ey} is the ohmic resistance of the YSZ electrolyte and L_{cables} takes into account the inductance of the cables connecting the cell to the EIS analyser.

The total impedance is schematically represented by the equivalent circuit reported in Fig. 2. It is worth reminding that the equivalent circuit represents the analytical solution of the physically-based model derived in this section, thus it is not a phenomenological circuit build *a posteriori* for the empirical interpretation of EIS data as commonly done in the literature.

Results and discussion

Samples, tests and measured parameters

The model described in Section 2 is used to interpret the impedance spectra of symmetric anodes prepared and tested by Somalu et al. [54,73]. The samples refer to cermet anodes made of Ni and ScSZ (more specifically, 10Sc1CeSZ), sintered at 1350 °C, with different solid volume fractions of Ni. Only the samples Ni30 and Ni40, corresponding to 30 and 40% vol. of Ni
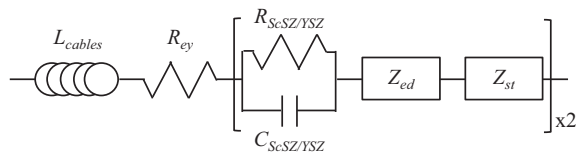
respectively, are considered: Ni30 is used as a benchmark for model calibration (Section 3.2) because it shows the largest impedance, thus allowing for a more accurate deconvolution, while Ni40 is used for verification purposes (Section 3.4). An additional sample, referred as 10x, is considered in Section 3.4. The sample 10x consists of a scaffold of ScSZ infiltrated 10 times with $Ni(NO_3)_2$ solution, following a fabrication procedure similar to that reported by Lomberg et al. [74]. Thus, in all the samples analysed in this study the materials are the same, only the electrode microstructure differs.

The impedance of the anodes was recorded over the frequency range 10^{-2}–10^5 Hz in an in-house built apparatus [73] using a symmetric setup at open-circuit over the temperature range 600−800 °C under 97% H_2−3% H_2O and 48.5% H_2−48.5% N_2−3% H_2O, referred in the following as 100% H_2 and 50% H_2.

The microstructural parameters required by the model are obtained from the analysis of the FIB-SEM reconstruction of the anodes after the tests (see Fig. 1b), as described by Tariq et al. [75,76]. Table 1 summarizes the microstructural parameters evaluated for Ni30 and used in Section 3.2. The effective conductivity of Ni in the samples was determined according to the van der Pauw technique with a 4-point probe [54,77]. The bulk ionic conductivity of ScSZ is taken from the literature [78] and approximated with the correlation:

$$\sigma_{ScSZ} = 6.5\cdot10^4\exp\left(-\frac{9250}{T}\right) \text{ S m}^{-1} \text{ within } 600-800\,°C \quad (21)$$

Calibration and deconvolution

The model is calibrated by comparing model simulations with experimental EIS data of Ni30 at different temperatures and hydrogen partial pressures. The calibration allows for the fitting of the unknown material-specific parameters related to the charge-transfer reactions at the electrode/electrolyte interface, $r_{ScSZ/YSZ}$ and $c_{ScSZ/YSZ}$, and at the distributed TPB, i_{OTPB} and $c_{Ni/ScSZ}$. The thickness of the stagnant layer L_{st} and the water molar fraction y_{H2O} are regarded as open fitting parameters of the diffusion model Z_{st}. Note that, although the water molar fraction is a known operating parameter, its value is allowed to vary in the simulations to take into account the complex three-dimensional convection and diffusion phenomena in the test rig which cannot be captured by a 1D diffusion model (Eq. (19)), as further discussed in Section 3.3.

Except for L_{st}, which is assumed constant in all the experimental conditions, the other parameters are expected to depend on temperature while being independent of hydrogen partial pressure. In addition, the material-specific parameters $r_{ScSZ/YSZ}$, $c_{ScSZ/YSZ}$, i_{OTPB} and $c_{Ni/ScSZ}$, are assumed to remain

Fig. 2 − **Schematic representation of the physically-based circuit model according to Eq. (20). In the figure, the following abbreviations are used: $R_{ScSZ/YSZ} = r_{ScSZ/YSZ}/A_{ScSZ/YSZ}$ and $C_{ScSZ/YSZ} = c_{ScSZ/YSZ}\cdot A_{ScSZ/YSZ}$.**

Table 1 − Microstructural parameters of sample Ni30.

Parameter	Value	Source
$A_{ScSZ/YSZ}$ [−]	0.5009	FIB-SEM
L_{TPB}^v [m m^{-3}]	$2.465\cdot10^{12}$	FIB-SEM
$A_{Ni/ScSZ}^v$ [m^2 m^{-3}]	$1.57\cdot10^6$	FIB-SEM
k_{ScSZ}^{eff} [−]	0.2569	FIB-SEM
σ_{Ni}^{eff} [S m^{-1}]	$6597.2 + 4.4533\cdot10^7/T$	Measured
L_{an} [μm]	30	SEM

constant in different electrode microstructures. A complex non-linear least square fitting is used to minimize the sum of squared residuals [79].

The calibration of the model for different operating temperatures is reported in Fig. 3. In the whole range of temperatures investigated, the spectra show two features in the Nyquist plot: a low-frequency contribution, which is almost unaffected by temperature, and a depressed feature at medium/high frequency, which shrinks as temperature increases. The model accurately reproduces the shape and frequency-dependence of experimental data, showing minor inaccuracies for frequencies <0.1 Hz.

Fig. 4 shows the comparison between model simulations and experimental data for different hydrogen partial pressures for the anode Ni30 at OCV and 700 °C. The Figure shows that increasing the hydrogen partial pressure affects only the low-frequency contribution, whose resistance is almost halved, while the feature at medium/high frequency remains unvaried. Also in this case, the model provides a satisfactory fitting of the experimental data, especially in the medium/high frequency range.

Besides reproducing the experimental data, the model allows for the physically-based deconvolution of the impedance spectra into three elementary contributions, as reported in Fig. 5a. The low-frequency (LF) contribution is due to the diffusion of gases in the stagnant layer, reproduced with Z_{st} according to Eq. (19). This interpretation is supported by the weak temperature-dependence of this feature (Fig. 3), the
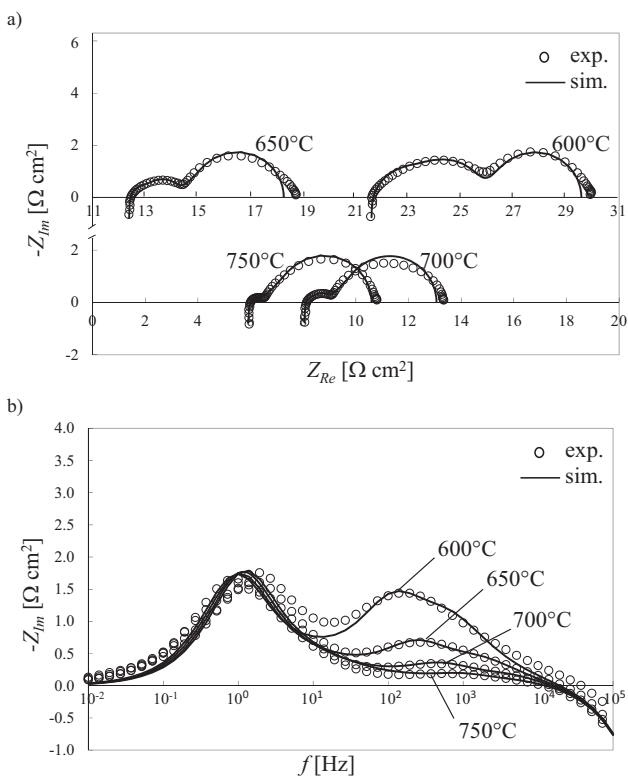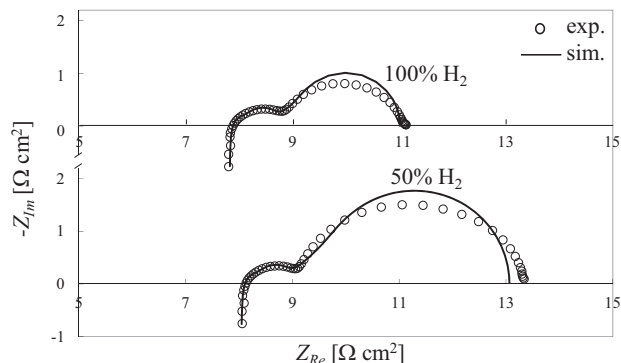

Fig. 4 – **Calibration of the physically-based model at different hydrogen partial pressures. The data refer to the cermet anode Ni30 at OCV and 700 °C.**

decrease in resistance as the hydrogen partial pressure increases (Fig. 4), and a characteristic frequency in the order of 1–5 Hz (see Fig. 3b) compatible with gas transport processes taking place in the test rig [55–57,72]. The large resistance associated to the LF is due to the arrangement of the test setup, as discussed in Section 3.3, and can be reduced with a proper design of the test rig.

The depressed feature at medium/high frequency is decoupled into two contributions: a medium-frequency feature (MF) and a smaller high-frequency feature (HF). The MF feature is associated to the electrochemical processes occurring along the anode thickness, described according to Z_{ed}. The frequency range is compatible with the distributed charge-transfer reaction as reported in the literature for similar electrodes [52,60,80]. This contribution is the one mostly affected by the microstructural properties of the electrode, since its impedance strongly depends on parameters such as L^v_{TPB}, $A^v_{Ni/ScSZ}$ and σ^{eff}_{ScSZ} according to Eq. (11). As anticipated in Section 2, gas diffusion across the anode thickness is not considered in Z_{ed}. This simplifying assumption is verified in the inset of Fig. 5a: the impedance of the MF feature is not affected when porous gas diffusion is included in the model according to the approach presented by Bertei et al. [81], thus porous gas diffusion can be neglected as done in Eq. (11). This is also corroborated by the findings of Ramos et al. [60], who report a negligible porous gas diffusion contribution in electrolyte-supported Ni:ScSZ functional layers.

Finally, the HF contribution is ascribed to the impedance Z_{Ot} of the oxygen transfer at the electrode/electrolyte interface (Eq. (2)), which is expected to be present in the high frequency range according to the literature [52,62,63,65]. The presence of three contributions in the experimental spectra is corroborated by the distribution of relaxation times (DRT), reported in Fig. 5b. The DRT method allows for the deconvolution of the spectra without any *a priori* assumptions, providing the resistance and characteristic frequency of each process. More details on the DRT method can be found elsewhere [82–84]. In this study the DRT is used as a semi-quantitative tool to corroborate the findings of the physically-based model. In particular, both the characteristic frequency and the resistance of each process identified with the DRT are compatible

Fig. 3 – **Calibration of the physically-based model at different temperatures. The data refer to the cermet anode Ni30 at OCV and 50% H$_2$. a) Nyquist plot; b) imaginary component of impedance versus frequency.**
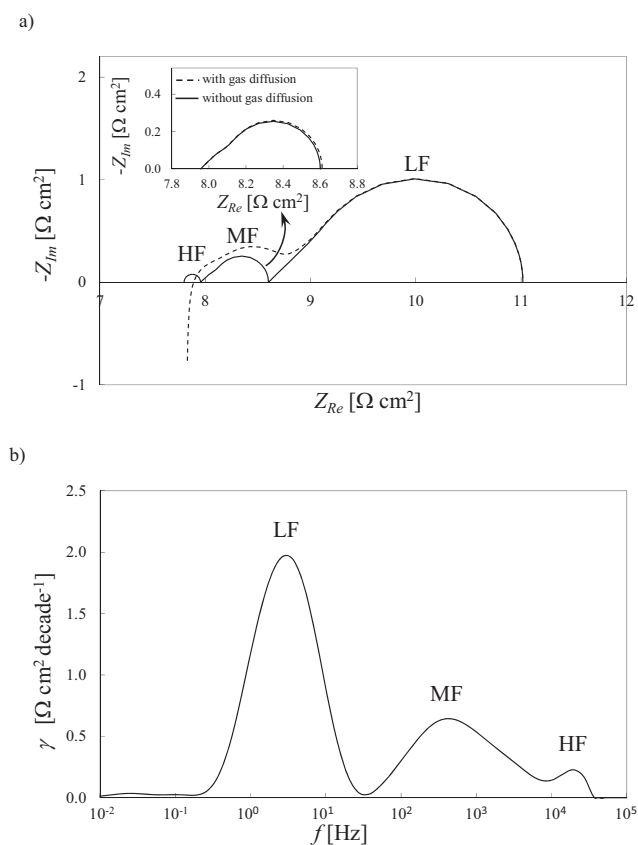
a)

b)

Fig. 5 – a) Deconvolution of impedance spectrum with the physically-based model, highlighting the three contributions to impedance in the Nyquist plot. The inset shows the comparison of the impedance of the medium-frequency process simulated with and without gas diffusion. b) DRT analysis of the experimental data, confirming the presence of three processes, in agreement with the physically-based model. Inductance was removed before calculating the DRT. Operating conditions: 700 °C, OCV, 100% H$_2$, sample Ni30.

with the independent deconvolution provided by the physically-based model in Fig. 5a. This is a good indication about the validity of the model proposed in this study, which is further discussed in the next section.

Discussion of fitted parameters

The calibration reported in Section 3.2 showed that the model satisfactorily reproduces the experimental impedance spectra in a wide range of operating conditions. However, before accepting the calibration as successful, the fitted parameters must be analysed and compared with the literature in order to assess their soundness.

The parameters fitted in Section 3.2 are summarized in Table 2 and reported in Fig. 6 as a function of temperature. Fig. 6 shows that all the material-specific parameters exhibit clear linear trends in the Arrhenius plot, which allow for the calculation of their activation energies, reported in Table 2.

The activation energy of i$_{OTPB}$, equal to 115 kJ mol^{-1}, is similar to what reported in the literature for Ni:ScSZ anode functional layers, i.e., 120 kJ mol^{-1} [85] and 111–122 kJ mol^{-1} [60]. In addition, this value compares reasonably well with the activation energy of the hydrogen charge-transfer in a very similar system, such as Ni:YSZ. For Ni:YSZ electrodes, de Boer [86] and Bieberle et al. [87] report an activation energy of 152 and 85 kJ mol^{-1}, respectively: in this study, the fitted $E_{act} = 115$ kJ mol^{-1} lies between these two extreme values. At 700 °C the i$_{OTPB}$ fitted in this study for Ni:ScSZ is equal to $46.0 \cdot 10^{-6}$ A m^{-1}, while in Ni:YSZ anodes the i$_{OTPB}$ is $27.5 \cdot 10^{-6}$ or $3.8 \cdot 10^{-6}$ A m^{-1} according to Bieberle et al. [87] or de Boer [86], respectively, for 97% H$_2$–3% H$_2$O. The ratio between the exchange current densities in Ni:ScSZ and Ni:YSZ lies between 1.67 (considering Bieberle et al. [87]) and 12.1 (considering de Boer [86]): this is in qualitative agreement with Shi et al. [85], who report an i$_{OTPB}$ in Ni:ScSZ about 5 times larger than in Ni:YSZ.

The resistance of the oxygen transfer $r_{ScSZ/YSZ}$ decreases sharply as the temperature increases (see Fig. 6). On the other hand, both the capacitances c$_{Ni/ScSZ}$ and c$_{ScSZ/YSZ}$ show a weak dependence on temperature as expected [18] and lie within the typical range 0.1–30 F m^{-2} reported in the literature [59,80,85,88]. Note that the fitted material-specific parameters do not vary with the hydrogen partial pressure within the range investigated, which is in fair agreement with the weak p_{H2}-dependence of the hydrogen electrochemical oxidation kinetics reported in the literature [86–89]. The effect of water partial pressure on the hydrogen electro-oxidation kinetic parameters, which can be more significant than p_{H2} according to Ramos et al. [60], will be subject of future analysis.

The thickness of the stagnant layer L_{st} remains constant with temperature and hydrogen partial pressure and is in the order of centimetres (see Table 2). This high value is attributed to the arrangement of the test rig and it is consistent with Aravind et al. [57], who used a similar experimental setup. However, the transport of gases in the test rig, ruled by a complex three-dimensional flow field, possibly influenced by pressure-driven flows [56,57], is expected to be more complex than the 1D diffusion considered in this study (see Eq. (19)). This supports the inaccuracies in the fitting of the LF feature in Section 3.2. Furthermore, this explains why the water molar fraction y$_{H2O}$ had to be left as an open fitting parameter during the calibration, as anticipated in Section 3.2. In particular, Table 2 shows that, in order to capture the LF resistance, y$_{H2O}$ must be reduced by about an order of magnitude if compared with the water molar fraction estimated from the operating conditions, equal to ca. 3%. Similar inaccuracies in the simulation of diffusion in the stagnant layer are acknowledged by Ramos et al. [60] too.

Hence, the model of gas diffusion in the stagnant layer Z$_{st}$ cannot be considered satisfactorily validated due to the complex geometry of the test rig. Nevertheless, it can be used to fit the LF feature and decouple its contribution from the total impedance in order to focus on the medium/high frequency range. On the other hand, the models of the HF and MF processes (Z$_{Ot}$ and Z$_{ed}$, respectively) and the corresponding parameters are robust and consistent with the literature. Since the microstructural contributions to impedance, which are the main target of this study, lie in the medium and high

Table 2 – List of parameters fitted for the sample Ni30. The activation energies, calculated according to the Arrhenius expression $v(T) = v_0 \exp\left(-\frac{E_{act}}{RT}\right)$, are reported in the last column.

Parameter	600 °C	650 °C	700 °C	750 °C	800 °C	E_{act} [kJ mol^{-1}]
$r_{ScSZ/YSZ}$ [Ω m^2]	$3.28 \cdot 10^{-5}$	$1.10 \cdot 10^{-5}$	$3.91 \cdot 10^{-6}$	$1.62 \cdot 10^{-6}$	$6.93 \cdot 10^{-7}$	−149
$c_{ScSZ/YSZ}$ [F m^{-2}]	6.99	8.62	9.98	11.14	13.34	23
i_{0TPB} [A m^{-1}]	$9.60 \cdot 10^{-6}$	$2.09 \cdot 10^{-5}$	$4.60 \cdot 10^{-5}$	$9.78 \cdot 10^{-5}$	$1.65 \cdot 10^{-4}$	115
$c_{Ni/ScSZ}$ [F m^{-2}]	0.27	0.27	0.27	0.27	0.27	0
L_{st} [m]			$1.05 \cdot 10^{-2}$			/
y_{H2O} [−]			0.0021 for 100%H$_2$, 0.0027 for 50% H$_2$			/

frequency range, the two models Z_{Ot} and Z_{ed} are verified in different electrode microstructures as discussed in the next section.

Model verification with different electrode microstructures

The quantification of the correlation between electrode microstructure and electrochemical performance requires the model to be tested in samples made with the same conducting materials but different microstructures. In this section the model presented in Section 2 and calibrated in Sections 3.2 and 3.3 is tested against the experimental EIS data of two different samples, namely Ni40 and 10x, referring to a cermet anode with 40% vol. of Ni and a ScSZ scaffold infiltrated 10 times with Ni, respectively, as presented in Section 3.1. As discussed in the previous sections, the contribution of the anode microstructure to impedance lies in the medium/high frequency range, thus only this region of the spectra is investigated in this section.

In order to corroborate the models Z_{Ot} and Z_{ed} in samples Ni40 and 10x, the following approach is used: the same material-specific parameters $r_{ScSZ/YSZ}$, $c_{ScSZ/YSZ}$, i_{0TPB} and $c_{Ni/ScSZ}$ reported in Table 2, obtained during the calibration of Ni30 (Section 3.2) and discussed in Section 3.3, are kept. Then, the microstructural parameters $A_{ScSZ/YSZ}$, L_{TPB}^{v}, $A_{Ni/ScSZ}^{v}$ and k_{ScSZ}^{eff} are fitted to reproduce the experimental impedance spectra of Ni40 and 10x. If the models Z_{Ot} and Z_{ed} and corresponding material-specific parameters are sound, the fitted microstructural properties will compare well with FIB-SEM results and will not vary with the operating temperature. Since the validation of the diffusion model of the stagnant layer Z_{st} is not the main concern here, the parameters L_{st} and y_{H2O} are
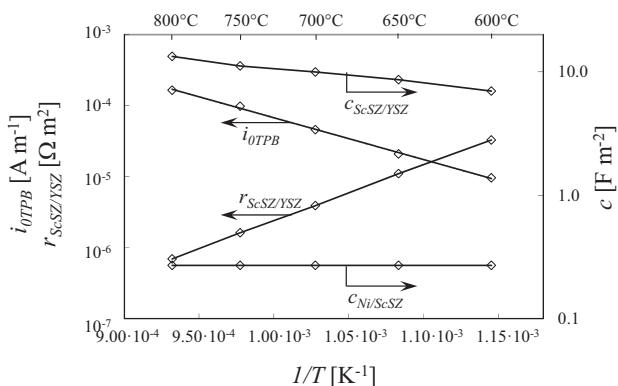
treated as open fitting parameters to reproduce the LF feature and are not subject to further discussion.

The comparison between model simulations and experimental data of samples Ni40 and 10x is reported in Figs. 7 and 8, respectively. As expected, the experimental impedance spectra in different samples differ in the medium/high frequency range, while the LF feature, ascribed to gas transport processes in the test rig, remains almost unaffected, which is consistent with the literature [60]. The Figures show that the model accurately reproduces the impedance in the medium/high frequency range for both samples Ni40 and 10x in different operating conditions.

Table 3 reports the microstructural parameters used to reproduce the spectra of Ni40 and 10x, in comparison with the microstructural parameters obtained through their FIB-SEM
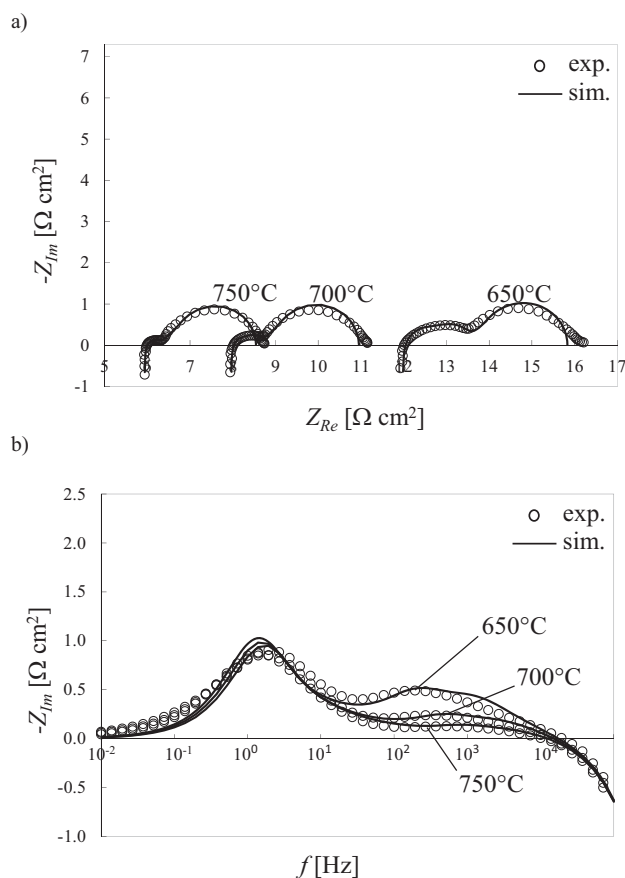
Fig. 7 – Model verification with cermet anode Ni40 for different temperatures at OCV and 50% H$_2$. a) Nyquist plot; b) imaginary component of impedance versus frequency.
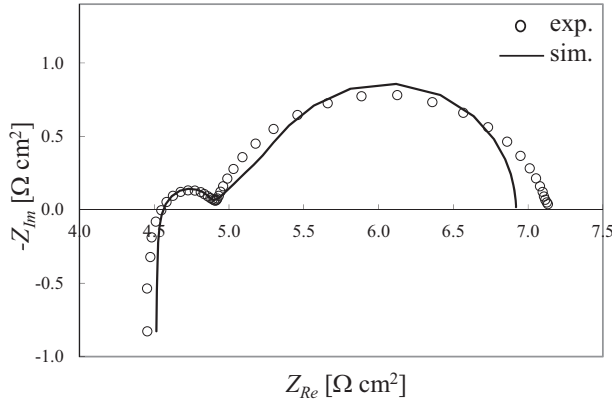
Fig. 6 – Arrhenius plot of the fitted parameters reported in Table 2. Note the different scales for left and right axis.

Fig. 8 – Model verification with infiltrated anode 10x at OCV, 700 °C and 50% H_2.

reconstruction. The analysis of Table 3 reveals some interesting insights.

For sample Ni40, the fitted value of L_{TPB}^v remains almost constant with temperature and is essentially coincident with the TPB density evaluated by FIB-SEM tomography. Similarly, the fitted normalized conductivity factor k_{ScSZ}^{eff} does not vary significantly with temperature and is only slightly larger than that obtained from the tomographic reconstruction of Ni40. Both these results are positive indications regarding the validity of the model. The fitted contact area $A_{Ni/ScSZ}^v$ shows some variability with temperature and is larger than the value of $1.74 \cdot 10^6$ m^{-1} obtained by FIB-SEM reconstruction. Since $A_{Ni/ScSZ}^v$ is coupled to $c_{Ni/ScSZ}$, which affects the characteristic frequency of charge-transfer reaction at the TPB, this variability reveals only the difficulty to reproduce the frequency-dependency of the MF feature, without undermining the general validity of the Z_{ed} model. Similarly, the interfacial area fraction $A_{ScSZ/YSZ}$, which is constant and smaller than 1, is larger than expected, since it should be equal to 0.361 according to the tomographic results reported in Table 3. This inaccuracy of the model is attributed to the difficulty of decoupling the oxygen transfer process, which represents a small contribution at high frequency, from the strongly overlapping feature associated with test rig inductance, as evident from Fig. 5a. Furthermore, this may indicate that the contact between electrode and the electrolyte is not ideal, as

assumed by the model. However, it is noteworthy that the fitted interfacial area fraction $A_{ScSZ/YSZ}$ is smaller than 1, which is the physical upper limit for the area fraction.

The analysis of the microstructural parameters obtained in anode 10x provides additional positive indications regarding the applicability of the model to electrodes with different microstructures. The interfacial area fraction $A_{ScSZ/YSZ}$, equal to 0.60, matches well with the estimated porosity ϕ of the ScSZ scaffold, which is ca. 40% [90], since ideally $A_{ScSZ/YSZ} \approx 1-\phi$ for a scaffold. In addition, the normalized conductivity factor of ScSZ k_{ScSZ}^{eff} is larger than in cermet electrodes as expected [91] and lies below the Hashin-Shtrikman upper bound of conductivity [92], confirming that it is realistic. The contact area $A_{Ni/ScSZ}^v$, equal to $0.9 \cdot 10^6$ m^{-1}, is similar to that measured in cermet electrodes Ni30 and Ni40. This result is credible because $A_{Ni/ScSZ}^v$ is proportional to the surface area per unit volume of the ScSZ scaffold, which is similar to that of ScSZ in cermet electrodes with the same volume fraction of scandia-stabilized zirconia as reported by Kishimoto et al. [90]. Finally, the TPB density L_{TPB}^v estimated in the infiltrated anode 10x is roughly one order of magnitude larger than the TPB length in cermet anodes, which is in good agreement with both experimental observations with FIB-SEM [90] and theoretical considerations [91,93].

Based on the good matching of EIS data in Figs. 7 and 8 as well as the considerations regarding the microstructural parameters, the validation of the model in samples Ni40 and 10x, prepared with different fabrication techniques and showing remarkably different microstructures, can be considered satisfactory.

As anticipated in Section 2, the model is not limited to Ni:ScSZ electrodes but can be used, in principle, for any anode made of a mixture of pure ion-conducting and pure electron-conducting materials. In the following, the model is applied to the cermet Ni:YSZ anode sintered at 1400 °C reported by Miyawaki et al. [94]. According to their experimental setup, a negligible oxygen transfer impedance Z_{Ot} is expected because they used the same ion-conducting material as electrolyte and within the electrode. In addition, the LF contribution, associated to the gas transport in the test rig, is minimal in their EIS spectra. Therefore, the Miyawaki et al. [94] data represent a useful benchmark to verify the electrode model Z_{ed}, which is the contribution mostly affected by microstructural properties as mentioned before.

According to the FIB-SEM reconstruction reported by Miyawaki et al. [94], the microstructural parameters of the cermet Ni:YSZ electrode are $L_{TPB}^v = 1.5 \cdot 10^{12}$ m^{-2}, $k_{YSZ}^{eff} = 0.093$ and $L_{an} = 8$ μm. In the operating conditions reported by the authors, i.e., 1000 °C and 97% H_2−3% H_2O, the bulk ionic conductivity of YSZ is 10.23 S m^{-1} [20,95] and the exchange current density i_{OTPB} is equal to $3.2 \cdot 10^{-4}$ A m^{-1} [86,87]. By applying Eq. (11) for $\omega = 0$ Hz, the calculated polarization resistance $R_{ed} = Z_{ed}(\omega = 0)$ is equal to 0.32 Ω cm^2. According to Miyawaki et al. [94], the experimental polarization resistance of the anode at 50 mA cm^{-2} (i.e., close to OCV) is about 0.34 Ω cm^2. Therefore, the model Z_{ed} presented in this paper provides a good prediction of the electrode polarization resistance also in Ni:YSZ anodes without adjusting or fitting any parameters.

Concluding, besides the reasonable trends of fitted parameters discussed in Section 3.3, the satisfactory verification with different microstructures and the positive application to Ni:YSZ

Table 3 – Microstructural parameters obtained in samples Ni40 and 10x by EIS fitting, compared with parameters evaluated in sample Ni40 with FIB-SEM reconstruction at room temperature. The thickness of the electrodes, measured with SEM, is 30 μm for Ni40 and 7.5 μm for 10x.

Parameter	FIB-SEM	Fitted Ni40			Fitted 10x
	Ni40	650 °C	700 °C	750 °C	700 °C
$A_{ScSZ/YSZ}$ [−]	0.361	0.74	0.74	0.74	0.60
L_{TPB}^v [m m^{-3}]	$3.86 \cdot 10^{12}$	$3.8 \cdot 10^{12}$	$4.0 \cdot 10^{12}$	$4.0 \cdot 10^{12}$	$23 \cdot 10^{12}$
$A_{Ni/ScSZ}^v$ [m^2 m^{-3}]	$1.74 \cdot 10^6$	$2.9 \cdot 10^6$	$2.6 \cdot 10^6$	$3.0 \cdot 10^6$	$0.9 \cdot 10^6$
k_{ScSZ}^{eff} [−]	0.126	0.13	0.15	0.15	0.38

anodes without any adjusted parameters confirm the reliability and good predictability of the model proposed in this study.

Conclusions

In this paper a physically-based model for the simulation of impedance spectra in SOFC anodes was presented, taking into account the main electrochemical and transport phenomena and their coupling with the electrode microstructure, reconstructed with FIB-SEM tomography. The model was calibrated to reproduce the EIS data of cermet Ni:ScSZ anodes in different operating conditions. The material-specific parameters obtained in the fitting, comprising the capacitance, the exchange current density and the activation energy of the hydrogen electrochemical oxidation, were in good agreement with values reported in the literature. The model was then validated in anodes with different microstructure, including an infiltrated electrode, and the fair prediction of the microstructural properties was confirmed by FIB-SEM tomography.

The study shows that the correlation between electrode microstructure and electrochemical performance can be addressed by using physically-based models, assisted by 3D tomography to provide the meaningful microstructural properties, and verified on impedance spectra for different microstructures. This approach turns out to be the most suitable to develop and validate interpretative and predictive modelling tools, capable to decouple the different contributions that build up the electrode resistance as well as to accurately infer kinetic and microstructural properties from impedance data, going beyond the capabilities of phenomenological equivalent circuits.

The model presented in this study and the corresponding material-specific parameters can be used to provide design indications to optimise the electrode microstructure or as a diagnostic tool to quantify the microstructural evolution upon application on EIS data at different stages of degradation. Further research will be dedicated to the extension of the model to simulate anode impedance under d.c. current and the corresponding effect of water partial pressure.

Acknowledgements

Nomenclature

$A^v_{Ni/ScSZ}$	contact area of Ni/ScSZ interface per unit volume (m^{-1})
$A_{ScSZ/YSZ}$	area of ScSZ/YSZ interface per unit of electrode area (−)
$c_{Ni/ScSZ}$	specific capacitance of the double-layer at Ni/ScSZ interface ($F\,m^{-2}$)
$c_{ScSZ/YSZ}$	specific capacitance associated the oxygen ion transfer at the ScSZ/YSZ interface ($F\,m^{-2}$)
D_i	average diffusivity of species i within the stagnant layer, with $i = 1, 2 = H_2, H_2O$ ($m^2\,s^{-1}$)
D_{ik}	binary diffusivity between gas species i and k ($m^2\,s^{-1}$)
E_{act}	activation energy ($J\,mol^{-1}$)
f	frequency (Hz)
F	Faraday constant ($C\,mol^{-1}$)
I	current density per unit of electrode area ($A\,m^{-2}$)
i_{0TPB}	exchange current density per unit of TPB length ($A\,m^{-1}$)
i_e	electronic current density ($A\,m^{-2}$)
$i^v_{Ni/ScSZ}$	current density of Ni/ScSZ double-layer per unit of electrode volume ($A\,m^{-3}$)
i_O	ionic current density ($A\,m^{-2}$)
i^v_{TPB}	Faradaic current density at TPB per unit of electrode volume ($A\,m^{-3}$)
j	imaginary unit (−)
k^{eff}_{Ni}	normalized conductivity factor of Ni phase (−)
k^{eff}_{ScSZ}	normalized conductivity factor of ScSZ phase (−)
L_{an}	anode thickness (m)
L_{cables}	inductance of the cables ($H\,m^2$)
L_{st}	thickness of the stagnant layer (m)
L^v_{TPB}	TPB length per unit volume (m^{-2})
N_i	molar flux of gas species i, with $i = 1, 2, 3 = H_2, H_2O, N_2$ ($mol\,m^{-2}\,s^{-1}$)
P	pressure (Pa)
R	gas constant ($J\,mol^{-1}\,K^{-1}$)
R_{ey}	ohmic resistance of the electrolyte ($\Omega\,m^2$)
$r_{ScSZ/YSZ}$	specific resistance of the oxygen ion transfer at the ScSZ/YSZ interface ($\Omega\,m^2$)
T	temperature (K)
V_{Ni}	potential of Ni phase (V)
V_{ScSZ}	potential of ScSZ phase (V)
x	coordinate along electrode thickness (m)
y_i	molar fraction of gas species i, with $i = 1, 2, 3 = H_2, H_2O, N_2$ (−)
Z	impedance of the cell ($\Omega\,m^2$)
Z_{ed}	impedance of the distributed charge-transfer and charge transport in the electrode ($\Omega\,m^2$)
Z_{Ot}	impedance of the oxygen ion transfer ($\Omega\,m^2$)
Z_{st}	impedance of the diffusion process in the stagnant layer ($\Omega\,m^2$)
Γ	dimensionless parameter defined in Eq. (8)
$\Delta\zeta$	phasor of the generic variable ζ
η	activation overpotential (V)
η_{conc}	concentration overpotential in the stagnant layer (V)
σ_{Ni}	bulk electric conductivity of Ni ($S\,m^{-1}$)
σ^{eff}_{Ni}	effective electric conductivity of Ni phase ($S\,m^{-1}$)
σ_{ScSZ}	bulk ionic conductivity of ScSZ ($S\,m^{-1}$)
σ^{eff}_{ScSZ}	effective ionic conductivity of ScSZ phase ($S\,m^{-1}$)
ϕ	porosity (−)
ω	angular frequency (Hz)
Ω	dimensionless parameter defined in Eq. (10)

Abbreviations

DRT	distribution of relaxation times

EIS   electrochemical impedance spectroscopy
FIB-SEM focused ion beam scanning electron microscope
HF   high-frequency feature
LF   low-frequency feature
MF   medium-frequency feature
Ni30   cermet Ni:ScSZ anode with 30% vol. of Ni
Ni40   cermet Ni:ScSZ anode with 40% vol. of Ni
OCV   open-circuit voltage
ScSZ   scandia-stabilized zirconia, more specifically
           10Sc1CeSZ
SOFC   solid oxide fuel cell
TPB   three-phase boundary
YSZ   yttria-stabilized zirconia
10x   infiltrated Ni:ScSZ anode impregnated 10 times with
           Ni

REFERENCES

[1] Singhal SC, Kendall K. High temperature solid oxide fuel cells: fundamentals, design and applications. Oxford: Elsevier; 2003.

[2] Larminie J, Dicks A. Fuel cell systems explained. New York: Wiley; 2003.

[3] Singhal SC. Advances in solid oxide fuel cell technology. Solid State Ionics 2000;135:305—13.

[4] Kee RJ, Zhu H, Goodwin DG. Solid-oxide fuel cells with hydrocarbon fuels. Proc Combust Inst 2005;30:2379—404. http://dx.doi.org/10.1016/j.proci.2004.08.277.

[5] Mogensen M, Skaarup S. Kinetic and geometric aspects of solid oxide fuel cell electrodes. Solid State Ionics 1996;86—88:1151—60. http://dx.doi.org/10.1016/0167-2738(96)00280-9.

[6] Yokokawa H, Tu H, Iwanschitz B, Mai A. Fundamental mechanisms limiting solid oxide fuel cell durability. J Power Sources 2008;182:400—12. http://dx.doi.org/10.1016/j.jpowsour.2008.02.016.

[7] Brus G, Miyoshi K, Iwai H, Saito M, Yoshida H. Change of an anode's microstructure morphology during the fuel starvation of an anode-supported solid oxide fuel cell. Int J Hydrogen Energy 2015;40:6927—34. http://dx.doi.org/10.1016/j.ijhydene.2015.03.143.

[8] Jiao Z, Lee G, Shikazono N, Kasagi N. Quantitative study on the correlation between solid oxide fuel cell Ni-YSZ composite anode performance and sintering temperature based on three-dimensional reconstruction. J Electrochem Soc 2012;159:F278—86. http://dx.doi.org/10.1149/2.056207jes.

[9] Golbert J, Adjiman CS, Brandon NP. Microstructural modeling of solid oxide fuel cell anodes. Ind Eng Chem Res 2008;47:7693—9. http://dx.doi.org/10.1021/ie800065w.

[10] Virkar AV, Chen J, Tanner CW, Kim J-W. The role of electrode microstructure on activation and concentration polarizations in solid oxide fuel cells. Solid State Ionics 2000;131:189—98. http://dx.doi.org/10.1016/S0167-2738(00)00633-0.

[11] Suzuki T, Hasan Z, Funahashi Y, Yamaguchi T, Fujishiro Y, Awano M. Impact of anode microstructure on solid oxide fuel cells. Science 2009;325:852—5. http://dx.doi.org/10.1126/science.1176404.

[12] Stockford C, Brandon N, Irvine J, Mays T, Metcalfe I, Book D, et al. H2FC SUPERGEN: an overview of the hydrogen and fuel cell research across the UK. Int J Hydrogen Energy 2015;40:5534—43. http://dx.doi.org/10.1016/j.ijhydene.2015.01.180.

[13] Brandon NP, Brett DJ. Engineering porous materials for fuel cell applications. Philos Trans A Math Phys Eng Sci 2006;364:147—59. http://dx.doi.org/10.1098/rsta.2005.1684.

[14] Haanappel VAC, Mertens J, Rutenbeck D, Tropartz C, Herzhof W, Sebold D, et al. Optimisation of processing and microstructural parameters of LSM cathodes to improve the electrochemical performance of anode-supported SOFCs. J Power Sources 2005;141:216—26. http://dx.doi.org/10.1016/j.jpowsour.2004.09.016.

[15] Tu H, Stimming U. Advances, aging mechanisms and lifetime in solid-oxide fuel cells. J Power Sources 2004;127:284—93. http://dx.doi.org/10.1016/j.jpowsour.2003.09.025.

[16] Kenney B, Karan K. Engineering of microstructure and design of a planar porous composite SOFC cathode: a numerical analysis. Solid State Ionics 2007;178:297—306. http://dx.doi.org/10.1016/j.ssi.2006.12.009.

[17] Zhang Y, Xia C, Ni M. Simulation of sintering kinetics and microstructure evolution of composite solid oxide fuel cells electrodes. Int J Hydrogen Energy 2012;37:3392—402. http://dx.doi.org/10.1016/j.ijhydene.2011.11.020.

[18] Bessler WG, Gewies S, Vogler M. A new framework for physically based modeling of solid oxide fuel cells. Electrochim Acta 2007;53:1782—800. http://dx.doi.org/10.1016/j.electacta.2007.08.030.

[19] Zhu H, Kee RJ. Modeling distributed charge-transfer processes in SOFC membrane electrode assemblies. J Electrochem Soc 2008;155:B715—29. http://dx.doi.org/10.1149/1.2913152.

[20] Bertei A, Mertens J, Nicolella C. Electrochemical simulation of planar solid oxide fuel cells with detailed microstructural modeling. Electrochim Acta 2014;146:151—63. http://dx.doi.org/10.1016/j.electacta.2014.08.120.

[21] Pramuanjaroenkij A, Kakaç S, Yang Zhou X. Mathematical analysis of planar solid oxide fuel cells. Int J Hydrogen Energy 2008;33:2547—65. http://dx.doi.org/10.1016/j.ijhydene.2008.02.043.

[22] Kanno D, Shikazono N, Takagi N, Matsuzaki K, Kasagi N. Evaluation of SOFC anode polarization simulation using three-dimensional microstructures reconstructed by FIB tomography. Electrochim Acta 2011;56:4015—21. http://dx.doi.org/10.1016/j.electacta.2011.02.010.

[23] Carraro T, Joos J, Rüger B, Weber A, Ivers-Tiffée E. 3D finite element model for reconstructed mixed-conducting cathodes: I. Performance quantification. Electrochim Acta 2012;77:315—23. http://dx.doi.org/10.1016/j.electacta.2012.04.109.

[24] Shearing PR, Cai Q, Golbert JI, Yufit V, Adjiman CS, Brandon NP. Microstructural analysis of a solid oxide fuel cell anode using focused ion beam techniques coupled with electrochemical simulation. J Power Sources 2010;195:4804—10. http://dx.doi.org/10.1016/j.jpowsour.2010.02.047.

[25] Shearing PR, Golbert J, Chater RJ, Brandon NP. 3D reconstruction of SOFC anodes using a focused ion beam lift-out technique. Chem Eng Sci 2009;64:3928—33. http://dx.doi.org/10.1016/j.ces.2009.05.038.

[26] Izzo JR, Joshi AS, Grew KN, Chiu WKS, Tkachuk A, Wang SH, et al. Nondestructive reconstruction and analysis of SOFC anodes using X-ray computed tomography at sub-50 nm resolution. J Electrochem Soc 2008;155:B504—8. http://dx.doi.org/10.1149/1.2895067.

[27] Wilson JR, Duong AT, Gameiro M, Chen H-Y, Thornton K, Mumm DR, et al. Quantitative three-dimensional microstructure of a solid oxide fuel cell cathode. Electrochem Commun 2009;11:1052—6. http://dx.doi.org/10.1016/j.elecom.2009.03.010.

[28] Joos J, Ender M, Rotscholl I, Menzler NH, Ivers-Tiffée E. Quantification of double-layer Ni/YSZ fuel cell anodes from

focused ion beam tomography data. J Power Sources 2014;246:819—30. http://dx.doi.org/10.1016/j.jpowsour.2013.08.021.

[29] Bertei A, Thorel AS, Bessler WG, Nicolella C. Mathematical modeling of mass and charge transport and reaction in a solid oxide fuel cell with mixed ionic conduction. Chem Eng Sci 2012;68:606—16. http://dx.doi.org/10.1016/j.ces.2011.10.025.

[30] Janardhanan VM, Deutschmann O. Numerical study of mass and heat transport in solid-oxide fuel cells running on humidified methane. Chem Eng Sci 2007;62:5473—86. http://dx.doi.org/10.1016/j.ces.2007.01.043.

[31] Zheng K, Li L, Ni M. Investigation of the electrochemical active thickness of solid oxide fuel cell anode. Int J Hydrogen Energy 2014;39:12904—12. http://dx.doi.org/10.1016/j.ijhydene.2014.06.108.

[32] Andersson M, Yuan J, Sundén B. Review on modeling development for multiscale chemical reactions coupled transport phenomena in solid oxide fuel cells. Appl Energy 2010;87:1461—76. http://dx.doi.org/10.1016/j.apenergy.2009.11.013.

[33] Chen D, Lin Z, Zhu H, Kee RJ. Percolation theory to predict effective properties of solid oxide fuel-cell composite electrodes. J Power Sources 2009;191:240—52. http://dx.doi.org/10.1016/j.jpowsour.2009.02.051.

[34] Costamagna P, Costa P, Antonucci V. Micro-modelling of solid oxide fuel cell electrodes. Electrochim Acta 1998;43:375—94.

[35] Bertei A, Nicolella C. Percolation theory in SOFC composite electrodes: effects of porosity and particle size distribution on effective properties. J Power Sources 2011;196:9429—36. http://dx.doi.org/10.1016/j.jpowsour.2011.06.087.

[36] Kenney B, Valdmanis M, Baker C, Pharoah JG, Karan K. Computation of TPB length, surface area and pore size from numerical reconstruction of composite solid oxide fuel cell electrodes. J Power Sources 2009;189:1051—9. http://dx.doi.org/10.1016/j.jpowsour.2008.12.145.

[37] Bertei A, Nucci B, Nicolella C. Microstructural modeling for prediction of transport properties and electrochemical performance in SOFC composite electrodes. Chem Eng Sci 2013;101:175—90. http://dx.doi.org/10.1016/j.ces.2013.06.032.

[38] Usseglio-Viretta F, Laurencin J, Delette G, Villanova J, Cloetens P, Leguillon D. Quantitative microstructure characterization of a Ni—YSZ bi-layer coupled with simulated electrode polarisation. J Power Sources 2014;256:394—403. http://dx.doi.org/10.1016/j.jpowsour.2014.01.094.

[39] Farhad S, Hamdullahpur F. Optimization of the microstructure of porous composite cathodes in solid oxide fuel cells. AIChE J 2012;58:1248—61. http://dx.doi.org/10.1002/aic.

[40] Ge X-M, Fang Y-N, Chan S-H. Design and optimization of composite electrodes in solid oxide cells. Fuel Cells 2012;12:61—76. http://dx.doi.org/10.1002/fuce.201100074.

[41] Ni M, Leung MKH, Leung DYC. Mathematical modeling of the coupled transport and electrochemical reactions in solid oxide steam electrolyzer for hydrogen production. Electrochim Acta 2007;52:6707—18. http://dx.doi.org/10.1016/j.electacta.2007.04.084.

[42] Bertei A, Barbucci A, Carpanese MP, Viviani M, Nicolella C. Morphological and electrochemical modeling of SOFC composite cathodes with distributed porosity. Chem Eng J 2012;207—208:167—74. http://dx.doi.org/10.1016/j.cej.2012.06.034.

[43] Kishimoto M, Lomberg M, Ruiz-Trejo E, Brandon NP. Numerical modeling of nickel-infiltrated gadolinium-doped ceria electrodes reconstructed with focused ion beam tomography. Electrochim Acta 2016;190:178—85. http://dx.doi.org/10.1016/j.electacta.2015.12.044.

[44] Bhattacharyya D, Rengaswamy R. A review of solid oxide fuel cell (SOFC) dynamic models. Ind Eng Chem Res 2009;48:6068—86. http://dx.doi.org/10.1021/ie801664j.

[45] Kakaç S, Pramuanjaroenkij A, Zhou XY. A review of numerical modeling of solid oxide fuel cells. Int J Hydrogen Energy 2007;32:761—86. http://dx.doi.org/10.1016/j.ijhydene.2006.11.028.

[46] Zhu H, Kee RJ, Janardhanan VM, Deutschmann O, Goodwin DG. Modeling elementary heterogeneous chemistry and electrochemistry in solid-oxide fuel cells. J Electrochem Soc 2005;152:A2427—40. http://dx.doi.org/10.1149/1.2116607.

[47] Jiang Y, Virkar AV. Fuel composition and diluent effect on gas transport and performance of anode-supported SOFCs. J Electrochem Soc 2003;150:A942—51. http://dx.doi.org/10.1149/1.1579480.

[48] Leonide A, Apel Y, Ivers-Tiffée E. SOFC modeling and parameter identification by means of impedance spectroscopy. ECS Trans 2009;19:81—109. http://dx.doi.org/10.1149/1.3247567.

[49] Yoon KJ, Gopalan S, Pal UB. Analysis of electrochemical performance of SOFCs using polarization modeling and impedance measurements. J Electrochem Soc 2009;156:B311—7. http://dx.doi.org/10.1149/1.3046158.

[50] Yurkiv V, Costa R, Ilhan Z, Ansar A, Bessler WG. Impedance of the surface double layer of LSCF/CGO composite cathodes: an elementary kinetic model. J Electrochem Soc 2014;161:F480—92. http://dx.doi.org/10.1149/2.070404jes.

[51] Yurkiv V, Utz A, Weber A, Ivers-Tiffée E, Volpp H-R, Bessler WG. Elementary kinetic modeling and experimental validation of electrochemical CO oxidation on Ni/YSZ pattern anodes. Electrochim Acta 2012;59:573—80. http://dx.doi.org/10.1016/j.electacta.2011.11.020.

[52] Bertei A, Arcolini G, Ouweltjes JP, Wuillemin Z, Piccardo P, Nicolella C. Physically-based deconvolution of impedance spectra: interpretation, fitting and validation of a numerical model for lanthanum strontium cobalt ferrite-based solid oxide fuel cells. Electrochim Acta 2016;208:129—41. http://dx.doi.org/10.1016/j.electacta.2016.04.181.

[53] Kromp A, Geisler H, Weber A, Ivers-Tiffée E. Electrochemical impedance modeling of gas transport and reforming kinetics in reformate fueled solid oxide fuel cell anodes. Electrochim Acta 2013;106:418—24. http://dx.doi.org/10.1016/j.electacta.2013.05.136.

[54] Somalu MR, Yufit V, Cumming D, Lorente E, Brandon NP. Fabrication and characterization of Ni/ScSZ cermet anodes for IT-SOFCs. Int J Hydrogen Energy 2011;36:5557—66. http://dx.doi.org/10.1016/j.ijhydene.2011.01.151.

[55] Primdahl S, Mogensen M. Gas diffusion impedance in characterization of solid oxide fuel cell anodes. J Electrochem Soc 1999;146:2827—33. http://dx.doi.org/10.1149/1.1392015.

[56] Bessler WG. Gas concentration impedance of solid oxide fuel cell anodes I. stagnation point flow geometry. J Electrochem Soc 2006;153:A1492—504. http://dx.doi.org/10.1149/1.2205150.

[57] Aravind PV, Ouweltjes JP, Schoonman J. Diffusion impedance on nickel/gadolinia-doped ceria anodes for solid oxide fuel cells. J Electrochem Soc 2009;156:B1417—22. http://dx.doi.org/10.1149/1.3231490.

[58] Bard AJ, Faulkner LR. Electrochemical methodes: fundamentals and applications. New York: Wiley; 2001.

[59] Zhu H, Kee RJ. Modeling electrochemical impedance spectra in SOFC button cells with internal methane reforming. J Electrochem Soc 2006;153:A1765—72. http://dx.doi.org/10.1149/1.2220065.

[60] Ramos T, Søgaard M, Mogensen MB. Electrochemical characterization of Ni/ScYSZ electrodes as SOFC anodes. J Electrochem Soc 2014;161:F434—44. http://dx.doi.org/10.1149/2.045404jes.

[61] Lasia A. Electrochemical impedance spectroscopy and its applications. New York, NY: Springer New York; 2014. http://dx.doi.org/10.1007/978-1-4614-8933-7.

[62] Adler SB, Lane JA, Steele BCH. Electrode kinetics of porous mixed-conducting oxygen electrodes. J Electrochem Soc 1996;143:3554—64. http://dx.doi.org/10.1149/1.1837252.

[63] Adler SB. Mechanism and kinetics of oxygen reduction on porous La1-xSrxCoO3-d electrodes. Solid State Ionics 1998;111:125—34. http://dx.doi.org/10.1016/S0167-2738(98)00179-9.

[64] Häffelin A, Joos J, Ender M, Weber A, Ivers-Tiffée E. Time-dependent 3D impedance model of mixed-conducting solid oxide fuel cell cathodes. J Electrochem Soc 2013;160:F867—76. http://dx.doi.org/10.1149/2.093308jes.

[65] Nielsen J, Klemensø T, Blennow P. Detailed impedance characterization of a well performing and durable Ni:CGO infiltrated cermet anode for metal-supported solid oxide fuel cells. J Power Sources 2012;219:305—16. http://dx.doi.org/10.1016/j.jpowsour.2012.07.031.

[66] Paasch G, Micka K, Gersdore P. Theory of the electrochemical impedance of macrohomogeneous porous electrodes. Electrochem Acta 1993;38:2653—62. http://dx.doi.org/10.1016/0013-4686(93)85083-B.

[67] Scribner Associates. ZView for windows. 2016.

[68] Sonn V, Leonide A, Ivers-Tiffée E. Combined deconvolution and CNLS fitting approach applied on the impedance response of technical Ni/8YSZ cermet electrodes. J Electrochem Soc 2008;155:B675—9. http://dx.doi.org/10.1149/1.2908860.

[69] Barsoukov E, Macdonald JR. Impedance spectroscopy: theory, experiment, and applications. 2nd ed. Hoboken, New Jersey: John Wiley & Sons; 2005. http://dx.doi.org/10.1002/0471716243.

[70] Krishna R, Wesselingh JA. The Maxwell-Stefan approach to mass transfer. Chem Eng Sci 1997;52:861—911. http://dx.doi.org/10.1016/S0009-2509(96)00458-7.

[71] Todd B, Young JB. Thermodynamic and transport properties of gases for use in solid oxide fuel cell modelling. J Power Sources 2002;110:186—200. http://dx.doi.org/10.1016/S0378-7753(02)00277-X.

[72] Primdahl S, Mogensen M. Gas conversion impedance: a test geometry effect in characterization of solid oxide fuel cell anodes. J Electrochem Soc 1998;145:2431—8. http://dx.doi.org/10.1149/1.1838654.

[73] Somalu MR. Fabrication and characterization of Ni/ScSZ cermet anodes for intermediate temperature SOFCs. UK: Imperial College London; 2012.

[74] Lomberg M, Ruiz-Trejo E, Offer G, Brandon NP. Characterization of Ni-infiltrated GDC electrodes for solid oxide cell applications. J Electrochem Soc 2014;161:F899—905. http://dx.doi.org/10.1149/2.0501409jes.

[75] Tariq F, Kishimoto M, Yufit V, Cui G, Somalu M, Brandon NP. 3D imaging and quantification of interfaces in SOFC anodes. J Eur Ceram Soc 2014;34:3755—61. http://dx.doi.org/10.1016/j.jeurceramsoc.2014.05.003.

[76] Tariq F, Kishimoto M, Cui G, Yufit V, Lomberg M, Ruiz-Trejo E, et al. Advanced 3D imaging and analysis of SOFC electrodes. ECS Trans 2015;68:2067—74. http://dx.doi.org/10.1149/06801.2067ecst.

[77] Rhazaoui K, Cai Q, Kishimoto M, Tariq F, Somalu MR, Adjiman CS, et al. Towards the 3D modelling of the effective conductivity of solid oxide fuel cell electrodes - validation against experimental measurements and prediction of electrochemical performance. Electrochim Acta 2015;168:139—47. http://dx.doi.org/10.1016/j.electacta.2015.04.005.

[78] Arachi Y, Sakai H, Yamamoto O, Takeda Y, Imanishai N. Electrical conductivity of the ZrO2-Ln2O3 (Ln = lanthanides) system. Solid State Ionics 1999;121:133—9. http://dx.doi.org/10.1016/S0167-2738(98)00540-2.

[79] Fu Y, Jiang Y, Poizeau S, Dutta A, Mohanram A, Pietras JD, et al. Multicomponent gas diffusion in porous electrodes. J Electrochem Soc 2015;162:F613—21. http://dx.doi.org/10.1149/2.0911506jes.

[80] Gewies S, Bessler WG. Physically based impedance modeling of Ni/YSZ cermet anodes. J Electrochem Soc 2008;155:B937—52. http://dx.doi.org/10.1149/1.2943411.

[81] Bertei A, Arcolini G, Nicolella C, Piccardo P. Effect of non-uniform electrode microstructure in gas diffusion impedance. ECS Trans 2015;68:2897—905. http://dx.doi.org/10.1149/06801.2897ecst.

[82] Schichlein H, Müller AC, Voigts M, Krügel A, Ivers-Tiffée E. Deconvolution of electrochemical impedance spectra for the identification of electrode reaction mechanisms in solid oxide fuel cells. J Appl Electrochem 2002;32:875—82. http://dx.doi.org/10.1023/A:1020599525160.

[83] Wan TH, Saccoccio M, Chen C, Ciucci F. Influence of the discretization methods on the distribution of relaxation times deconvolution: implementing radial basis functions with DRTtools. Electrochim Acta 2015;184:483—99. http://dx.doi.org/10.1016/j.electacta.2015.09.097.

[84] Boukamp BA. Fourier transform distribution function of relaxation times; application and limitations. Electrochim Acta 2015;154:35—46. http://dx.doi.org/10.1016/j.electacta.2014.12.059.

[85] Shi Y, Cai N, Li C, Bao C, Croiset E, Qian J, et al. Simulation of electrochemical impedance spectra of solid oxide fuel cells using transient physical models. J Electrochem Soc 2008;155:B270—80. http://dx.doi.org/10.1149/1.2825146.

[86] De Boer B. SOFC anode: hydrogen oxidation at porous nickel and nickel/yttria-stabilized zirconia cermet electrodes. The Netherlands: University of Twente; 1998.

[87] Bieberle A, Meier LP, Gauckler LJ. The electrochemistry of Ni pattern anodes used as solid oxide fuel cell model electrodes. J Electrochem Soc 2001;148:A646—56. http://dx.doi.org/10.1149/1.1372219.

[88] Bessler WG, Vogler M, Störmer H, Gerthsen D, Utz A, Weber A, et al. Model anodes and anode models for understanding the mechanism of hydrogen oxidation in solid oxide fuel cells. Phys Chem Chem Phys 2010;12:13888—903. http://dx.doi.org/10.1039/c0cp00541j.

[89] Utz A. The electrochemical oxidation of H2 and CO at patterned Ni anodes of SOFCs. Germany: Karlsruher Institut für Technologie (KIT); 2011.

[90] Kishimoto M, Lomberg M, Ruiz-Trejo E, Brandon NP. Enhanced triple-phase boundary density in infiltrated electrodes for solid oxide fuel cells demonstrated by high-resolution tomography. J Power Sources 2014;266:291—5. http://dx.doi.org/10.1016/j.jpowsour.2014.05.038.

[91] Bertei A, Pharoah JG, Gawel DAW, Nicolella C. A particle-based model for effective properties in infiltrated solid oxide fuel cell electrodes. J Electrochem Soc 2014;161:F1243—53. http://dx.doi.org/10.1149/2.0931412jes.

[92] Chueh CC, Bertei A, Pharoah JG, Nicolella C. Effective conductivity in random porous media with convex and non-convex porosity. Int J Heat Mass Transf 2014;71:183—8. http://dx.doi.org/10.1016/j.ijheatmasstransfer.2013.12.041.

[93] Hardjo EF, Monder DS, Karan K. An effective property model for infiltrated electrodes in solid oxide fuel cells. J Electrochem Soc 2014;161:F83—93. http://dx.doi.org/10.1149/2.036401jes.

[94] Miyawaki K, Kishimoto M, Iwai H, Saito M, Yoshida H. Comprehensive understanding of the active thickness in solid oxide fuel cell anodes using experimental, numerical and semi-analytical approach. J Power Sources 2014;267:503—14. http://dx.doi.org/10.1016/j.jpowsour.2014.05.112.

[95] Nam JH, Jeon DH. A comprehensive micro-scale model for transport and reaction in intermediate temperature solid oxide fuel cells. Electrochim Acta 2006;51:3446—60. http://dx.doi.org/10.1016/j.electacta.2005.09.041.